ISSN 0016-8521, Geotectonics, 2017, Vol. 51, No. 3, pp. 259–278. © Pleiades Publishing, Inc., 2017.
Original Russian Text © A.N. Moskalenko, A.K. Khudoley, R.R. Khusnitdinov, 2017, published in Geotektonika, 2017, No. 3, pp. 61–82.

Stress State Reconstruction and Tectonic Evolution of the Northern Slope of the Baikit Anteclise, Siberian Craton, Based on 3D Seismic Data

A. N. Moskalenko[a], *, A. K. Khudoley[a], and R. R. Khusnitdinov[b]

[a] *St. Petersburg State University, St. Petersburg, Universitetskaya nab. 7/9, 199034, Russia*
[b] *LLC GAZPROMNEFT STC, St. Petersburg, ul. Naberezhnaya reki Moiki 75–79, 190000, Russia*
**e-mail: artemmn@gmail.com*

Received November 20, 2016

Abstract—In this work, we consider application of an original method for determining the indicators of the tectonic stress fields in the northern Baikit anteclise based on 3D seismic data for further reconstruction of the stress state parameters when analyzing structural maps of seismic horizons and corresponded faults. The stress state parameters are determined by the orientations of the main stress axes and shape of the stress ellipsoid. To calculate the stress state parameters from data on the spatial orientations of faults and slip vectors, we used the algorithms from quasiprimary stress computation methods and cataclastic analysis, implemented in the software products FaultKinWin and StressGeol, respectively. The results of this work show that kinematic characteristics of faults regularly change toward the top of succession and that the stress state parameters are characterized by different values of the Lode–Nadai coefficient. Faults are presented as strike-slip faults with normal or reverse component of displacement. Three stages of formation of the faults are revealed: (1) partial inversion of ancient normal faults, (2) the most intense stage with the predominance of thrust and strike-slip faults at north-northeast orientation of an axis of the main compression, and (3) strike-slip faults at the west-northwest orientation of an axis of the main compression. The second and third stages are pre-Vendian in age and correlate to tectonic events that took place during the evolution of the active southwestern margin of the Siberian Craton.

Keywords: local stress state, stress fields, slip vector, seismic horizon, southwestern Siberian Craton
DOI: 10.1134/S0016852117030086

INTRODUCTION

Studies of stress state parameters is an important problem in paleotectonic reconstructions and simulations of regional evolutions (see [2, 8, 9, 17, 21, 22, 34–37, 39, 45], etc.). Methods for reconstructing stress state parameters are based on the principles of transition from structural–kinematic data on faults and fractures to the parameters of stress tensors [15, 16].

Traditionally, field methods for reconstructing stress state parameters are based on distinguishing conjugate fractures, fault planes with slickensides and slickenlines, joints, or a combination of these features with the employment of additional data on other small structural forms (see [4–7, 12, 14, 16, 19, 29, 31–33, 41], etc.). The present-day stress field is reconstructed by methods based on information about earthquake focal mechanisms (see [1] and overview of methods in [16, 43]).

However, studies devoted to the methods of investigating the stress state of the Earth's crust from indirect data are sparse. These methods are most applicable to territories characterized by an absence of natural outcrops and/or located in zones of low seismic activity. These methods are, first of all, the deciphering of topographic maps of various scales (see, e.g., [18, 20]) and the method of determining the stress state from displacements identified on surfaces of seismic horizons via reconstruction of the prefaulting positions of seismic boundaries relative to each other [34]. In this work, we used a structural geological method of determining the stress state parameters based on analysis of structural maps of 3D seismic horizons obtained by the seismic reflection method with a common depth point, where the tectonic stress indicator is the vector of slip (displacement) along a fault. This is a refinement of the method proposed by A.P. Gartrell [34] and was developed by the authors; it has already been applied when studying the Urman-Archa oil production area in Western Siberia [11]. The main aim of this work was to apply this method for stress state reconstruction for an object with a different tectonic setting with dominant oblique reverse faulting slips, in contrast to oblique normal faulting slips revealed for the Urman-Archa oil production area [11]. As an exam-

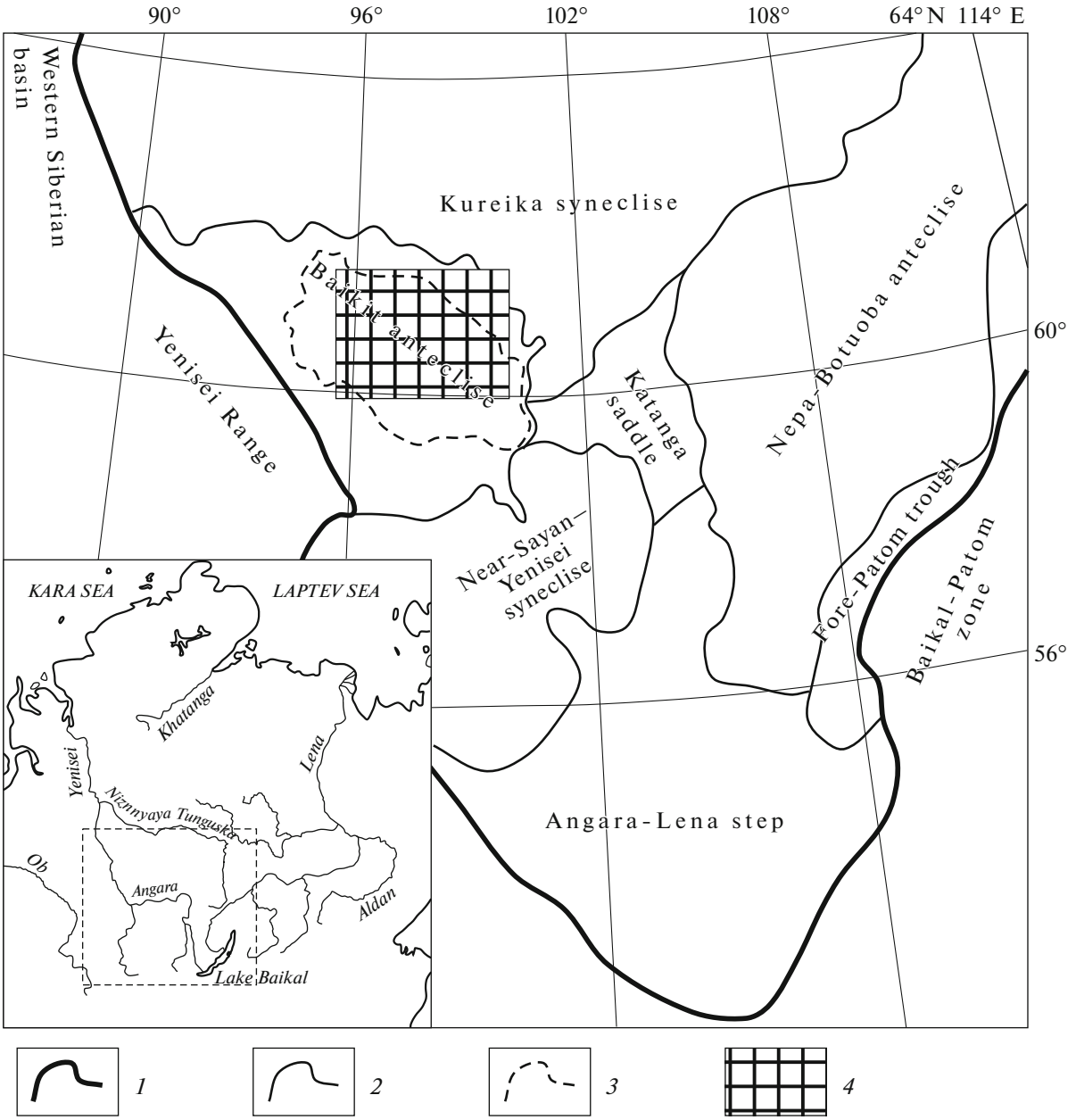

Fig. 1. Tectonic scheme of study area, after [26], with modifications by authors. (*1*) Siberian Craton boundary; (*2*) boundaries of main structures; (*3*) Kuyumba dome boundary; (*4*) study area. Location of studied region is shown in the inset map.

ple, we used the data on the Riphean complex in the northern limb of the Baikit anteclise. It should be noted that similar approaches were also proposed in [40, 42], but the former only used the method for determining the slip vector without subsequent interpretation and the latter mainly focused on strain analysis from the amplitudes of displacements along fault planes.

GEOLOGICAL SETTING

The study area is located in the southwestern Siberian Craton, in the interfluve of Podkamennaya Tunguska River. In terms of tectonics, it is located in the northeastern Baikit anteclise and southern Kureika syneclise (Fig. 1).

The sedimentary cover in the study area overlay the Archean–Lower Proterozoic basement and is represented by Riphean–Cambrian deposits. In this work, we will mainly consider the Riphean complex.

Based on the interpretation of deep seismic transects SB-1 ("Batholith") and SB-3 ("Altay–Severnaya Zemlya"), the Baikit anteclise is a gently sloping weakly asymmetric NW-oriented structure [27]. The largest regional structure is the Kamo dome, whose structure changes along its course from nearly symmetric gently sloped anticline to a rise confined by steeply dipping

faults. In the central part of the Kamo dome, the Kuyumba (near-dome) ENE-oriented rift and the Baikit and Engida marginal outliers (rift branches) are identified [26]. In the sedimentary cover cross section, several large seismic megacomplexes are distinguished; they correspond to the sedimentation cycles, marking the gradual filling of grabens and widening of the sedimentation basin beyond their limits. During the Riphean, sedimentation in the Baikit anteclise took place under the setting of consedimentation slopes prograding southwards and northeastwards [27].

We assumed the scheme of stratigraphic subdivision of Riphean deposits in the Baikit anteclise (Fig. 2), which is based mainly on the data by E.M. Khabarov [24, 25], V.V. Kharakhinov, and S.I. Shlenkin [26]. The age of the cross section is determined by presence of basic-rock sills with an Ar–Ar age of around 1500 Ma which cut Zelendukon sandstones and by the fact that the carbonate part of the cross section is referred to the Middle Riphean based on the strontium and carbon isotope characteristics [24–26]. A considerable number of hiatuses and unconformities are revealed, with the most significant being the discordant beddings at the bases of the Yurubchen, Kopchera, Vingol'da, and Tokur strata. Judging from the data provided by E.M. Khabarov [25], the largest sedimentation hiatuses (at least 100 Ma long) fall in the periods when the pre-Yurubchen and pre-Kopchera unconformities formed.

Vendian strata are characterized by subhorizontally position and, at their base, overlap different Riphean strata (locally, also crystalline basement rocks) with an angular unconformity. Although the dip angles of Riphean rocks are generally insignificant, they are up to 30°–50° in the near-fault zones [25, 26]. The Riphean complex is partitioned by faults with displacement amplitudes of more than 1 km and which are also overlain by Vendian rocks. In the Vendian complexes, these faults are not observed. The deformation time is limited to the age of the youngest Riphean rocks (about 1000 Ma) and to Vendian age. Taking into account the common distribution of thrusts, these deformations were most likely associated with accretionary and collisional events that took place on the adjacent margin of the Siberian Craton exposed in the Yenisei Range. Here, transformation of the passive margin into active one occurred at ca. 800 Ma and, judging by the ages of collisional granites and metamorphism, the most intense deformations occurred at ca. 760–750 and 685–600 Ma [3].

DESCRIPTION OF THE METHOD

When studying the stress state parameters for the Riphean complex in the study area, we used the method of determining the kinematic characteristics of faults from analyzing the 3D seismic data (Fig. 3). In the structural map of the reflecting horizon, we selected a characteristic landform (positive for anticline or negative for anticline) identified both in the hanging and foot wall of the fault. For the chosen structure, the trace of its axial surface was outlined in the map (this trace is pierced when the fault crosses this structure). We determined the coordinates for the points where the axial surface trace is pierced, whereas the vector joining the separated fragments of the structure is the slip vector (displacement). Using the available software tools, we determined the occurrence elements of the fault fragment within which the slip vector is located; this eventually determined both the total kinematic characteristics of the fault and the amplitude of displacement along it (see Fig. 3). In this case, the respective fragment of the fault and the slip vector located on it can be considered as analogs of slickenside surfaces and slickenlines on the fault planes, so their further processing can use similar methods.

Reconstruction of stress state parameters in this approach implies the following four stages:

(1) selection of structural maps of seismic horizons for further structural–geological reconstructions;

(2) determination of the kinematic characteristics of faults from analysis of the structural maps of seismic horizons;

(3) creation of a database containing the characteristics of faults and slip vectors;

(4) reconstruction of the stress state parameters.

Initial Data

The main data source for calculating the stress state parameters involves structural maps of seismic horizons obtained by the 3D SRM–CDP method and containing the faults interpreted in them. Structural maps were chosen in association with LLC GAZPROMNEFT STC. For further interpretation, we selected three seismic horizons which are interpreted with highest confidence (upsection): R_4 (at the base of the Madra stratum), R_3 (near the top of the Kopchera stratum), and R_2, (near the base of the Tokur stratum) (see Fig. 2). These horizons contain faults with determinable kinematic characteristics that is necessary for further reconstruction of stress fields.

Determination of the Fault Kinematics

The slip vectors were determined from structural maps of the R_4, R_3, and R_2 seismic horizons interpreted in the Riphean cross section (Figs. 4–6). It should be noted that this method of slip vectors determination is largely subjective, because anticline and syncline structures that could be unambiguously identified and correlated on both fault walls are quite rare. In order to increase the reliability of their identification, surface maps of the seismic horizons were analyzed by two ways: (a) manual drawing of the axial surface trace on an isoline map of differences in altitude; (b) on a map showing the surface curvature of the seis-

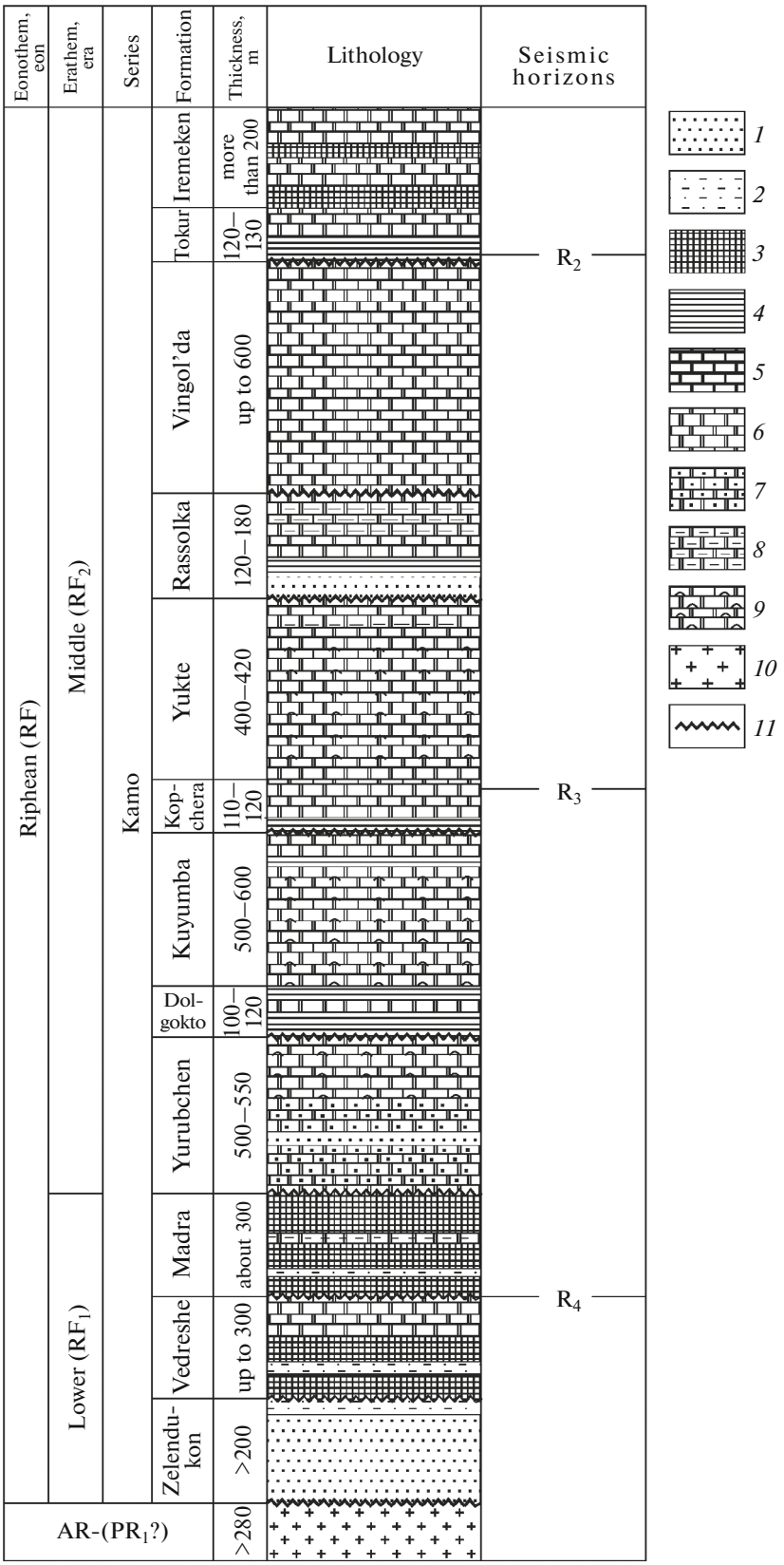

Fig. 2. Stratigraphic section of northern Baikit anteclise, after [24–26], with additions by authors. (*1*) Sandstones, (*2*) siltstones, (*3*) organic-rich mudstones, (*4*) mudstones, (*5*) limestones, (*6*) dolomites, (*7*) sandy dolomites, (*8*) silty dolomites, (*9*) stromatolite dolomites, (*10*) crystalline basement, (*11*) unconformity.

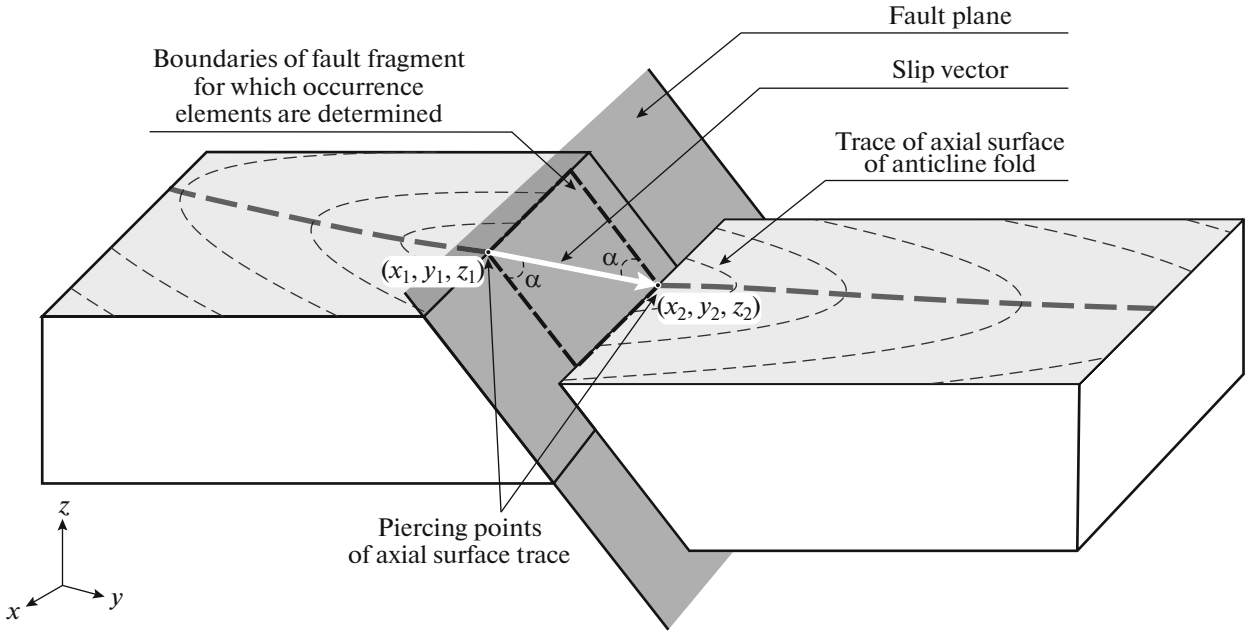

Fig. 3. Scheme of slip vector determination from fault parameters. Angle α is acute angle between slip vector and direction of fault plane dipping; its determines the ratio between normal or reverse faulting and strike-slip components.

mic horizon. The more rigourous method of drawing the axial surface trace implies visual analysis of the morphology of seismic horizons and tracking of similar structures in both the hanging wall and footwall of the fault. The difference in depth between adjacent isolines is 50 m, so in many cases, fold structures are not very clearly identified. In order to obtain a clearer drawing of the structure from whose displacement it is possible to determine the slip vector, the interval between isolines was reduced to 30 m, because resolving power of the seismic data is 25–30 m. Sometimes, for more accurate location of piercing points in the axial surface trace, fragments of the seismic horizon surface were considered at some angle to the horizontal plane, with the vertical scale increased relative to the horizontal (Fig. 7a). However, the second drawing method mathematically calculates the curvature coefficient for the seismic horizon surface, where the maximum values of the surface curvature coefficient correspond to the case of the axial surface trace of an anticline in a syncline structure. Importantly, the use of displacement of the axial surface trace to infer the kinematic characteristics of a fault is possible only if this fault had cut the already formed folds. Faults cut fold structures whose orientations are close to perpendicular relative to these faults; the fault surfaces remain unchanged and did not undego folded deformations (see Fig. 7). These considerations help us to conclude that in the selected examples faults formed after folds.

After all slip vectors are determined, the observation points and vectors proper are drawn on the map with subsequent checking of the reliability of data according to two main criteria: (1) a similar kinematics should be observed at different horizons for the same fault or a segment of it (e.g., fault segments where right-lateral strike-slip was identified at the R_3 horizon, while left-lateral strike-slip at the R_2 and R_4 horizons were excluded from further consideration); (2) the kinematic characteristics should not change frequently within the limits of one fault (in particular, we excluded from further consideration faults and fragments within whose limits right- and left-lateral strike-slip alternated in an irregular manner). Nevertheless, we took into consideration the fact that oppositely directed strike-slip could be a response to thrusting for curvilinear faults [44].

Creation of Databases

After sorting out the insufficiently reliable slip vectors, the data on the kinematic characteristics of faults were summarized in a database (Table 1), which contained the following measurement characteristics used for stress state reconstruction:

(1) number of measurement on the map;

(2) occurrence elements of a fault fragment;

(3) occurrence elements of a slip vector;

(4) orientation of a slip vector in the fault plane (rake);

(5) angle α showing the deviation of a slip vector from the fault plane, i.e., indicating the value of shear component (see Fig. 2);

(6) fault type (right-lateral strike-slip, normal fault, etc.);

(7) characteristics of the value of a slip vector (vertical, horizontal, and total displacement).

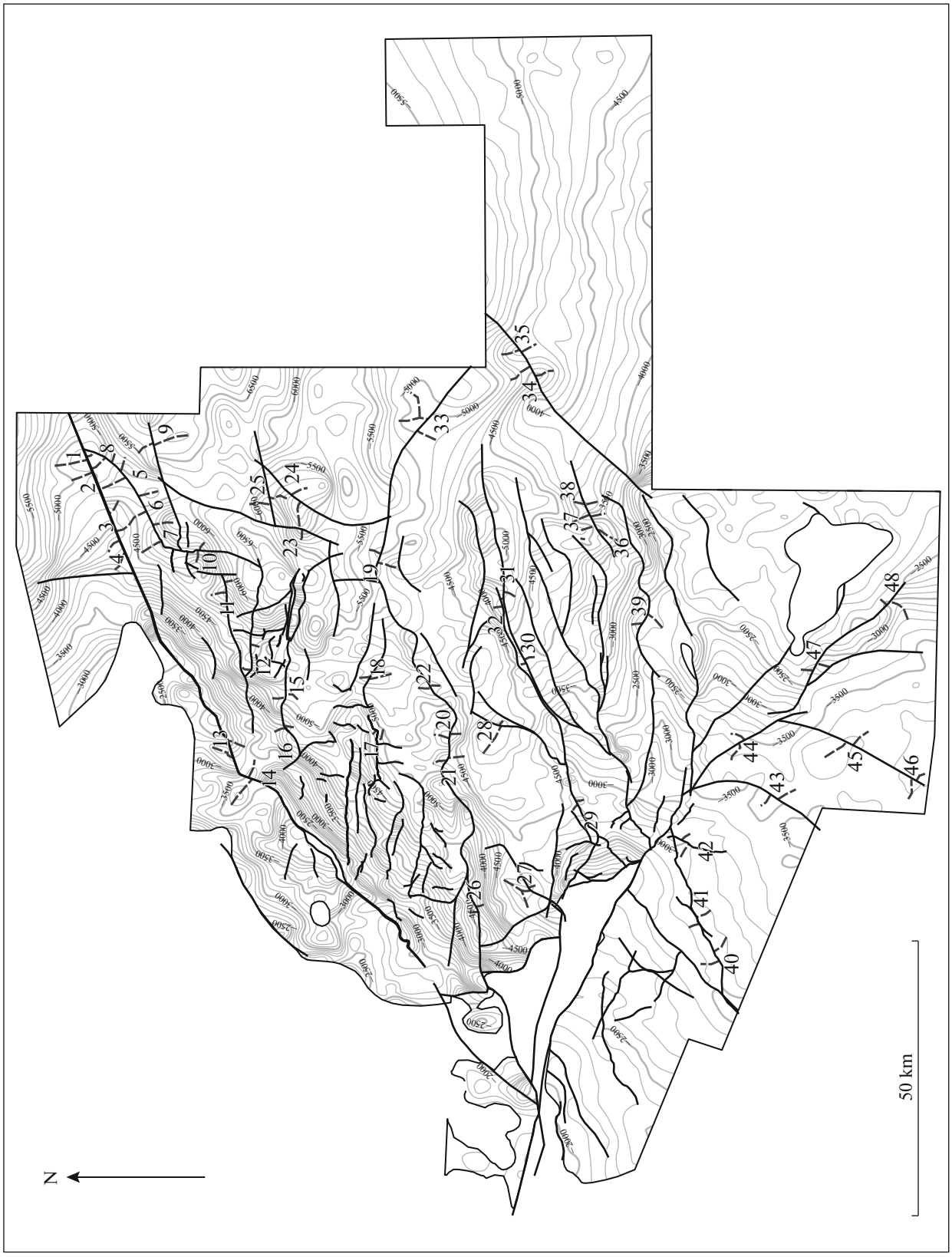

Fig. 4. Seismic horizon R_4 with indicated locations of measurements and numbers of slip vectors. Faults are represented as black lines. Slip vector numbers correspond to those in Table 1.

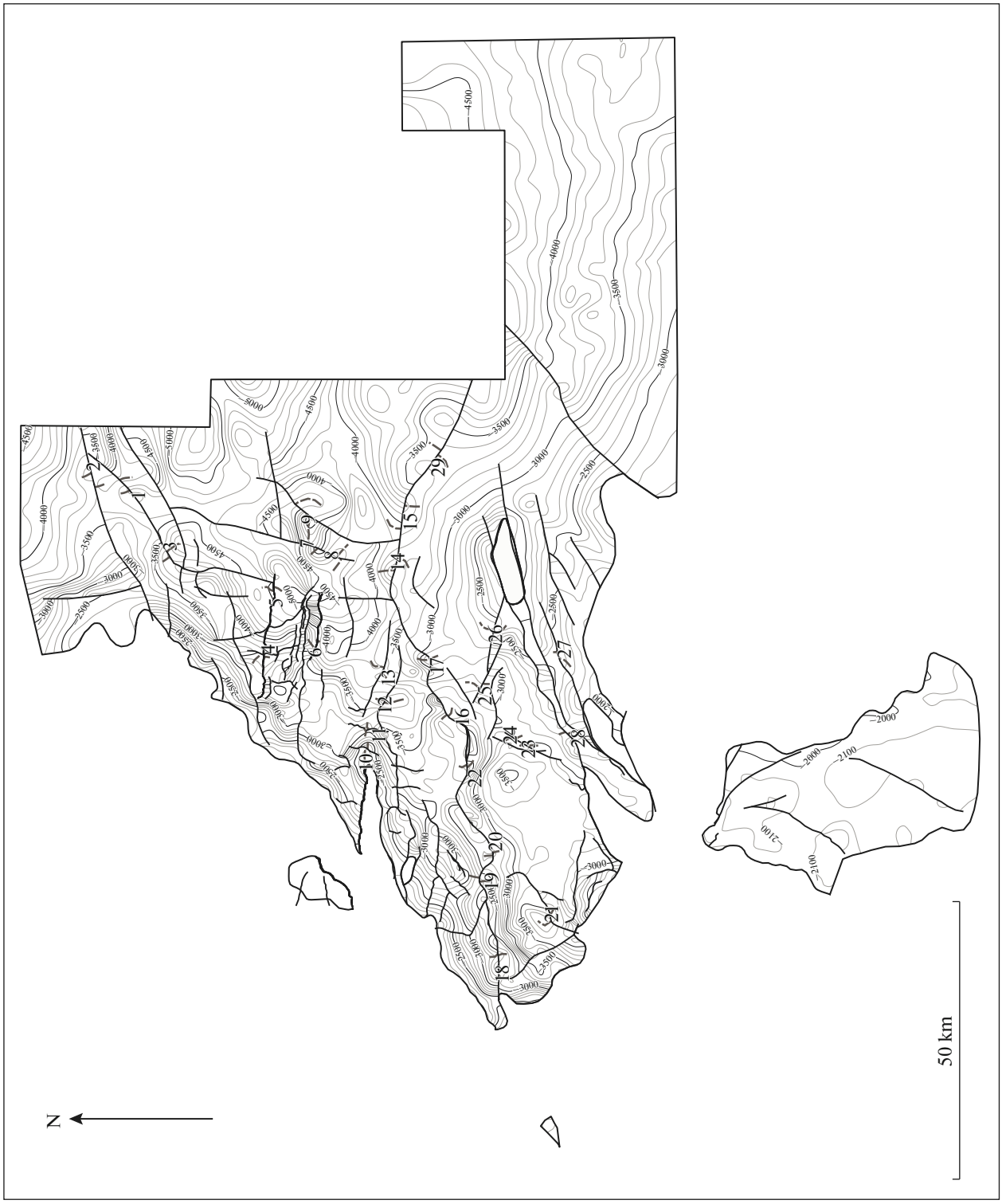

Fig. 5. Seismic horizon R_3 with indicated locations of measurements and numbers of slip vectors. Faults are represented as black lines. Slip vector numbers correspond to those in Table 1.

Reconstruction of Stress State Parameters

To calculate the stress state parameters from the data on spatial orientation of fault and slip vectors, we used calculation algorithms from quasiprimary stresses and cataclastic analysis methods. Since there are compressive stresses almost everywhere at crustal depths due to the effect of mass forces, we used the following indices and names for main stress axes: axis of maximum stress

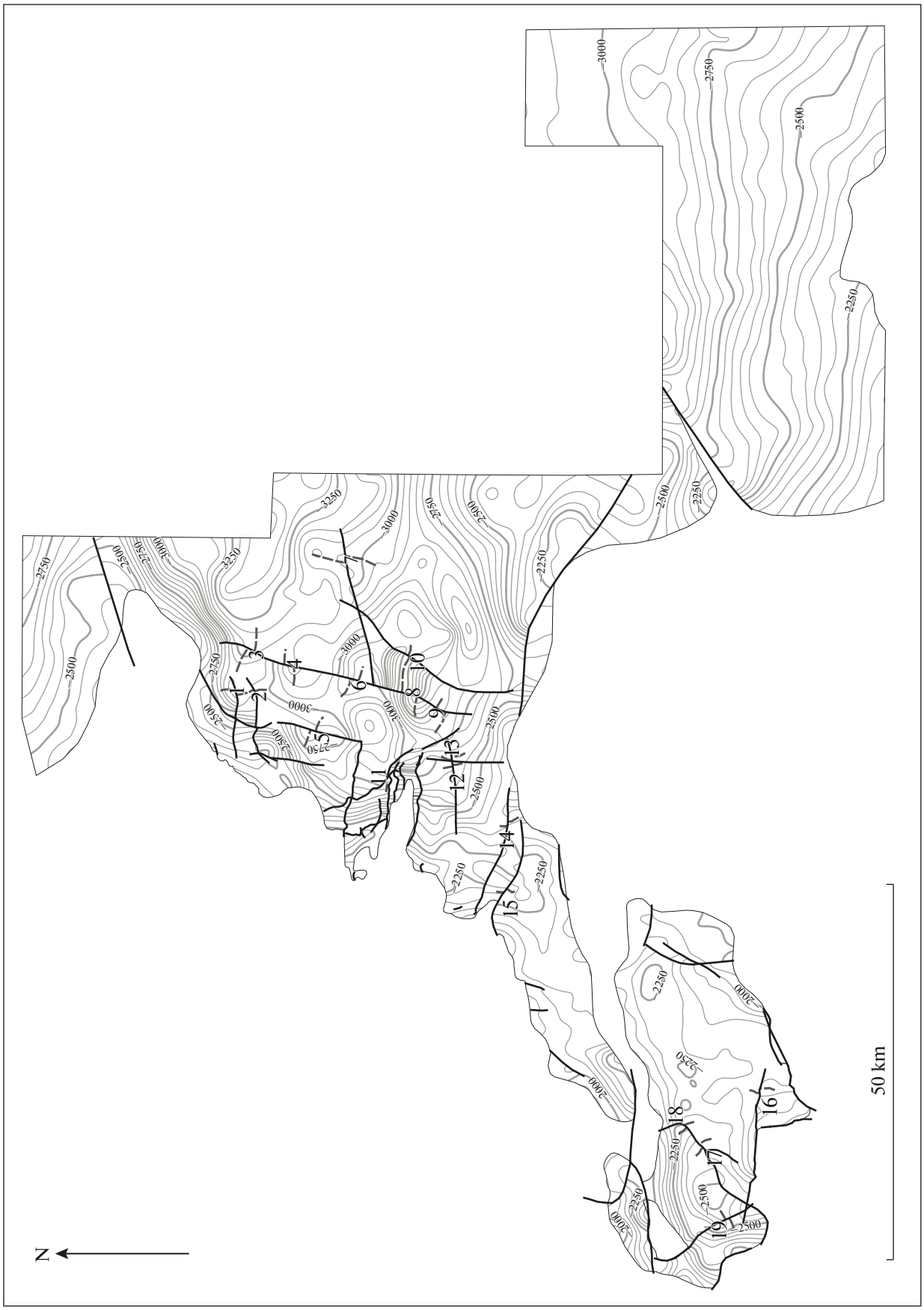

Fig. 6. Seismic horizon R_2 with indicated locations of measurements and numbers of slip vectors. Faults are represented as black lines. Slip vector numbers correspond to those in Table 1.

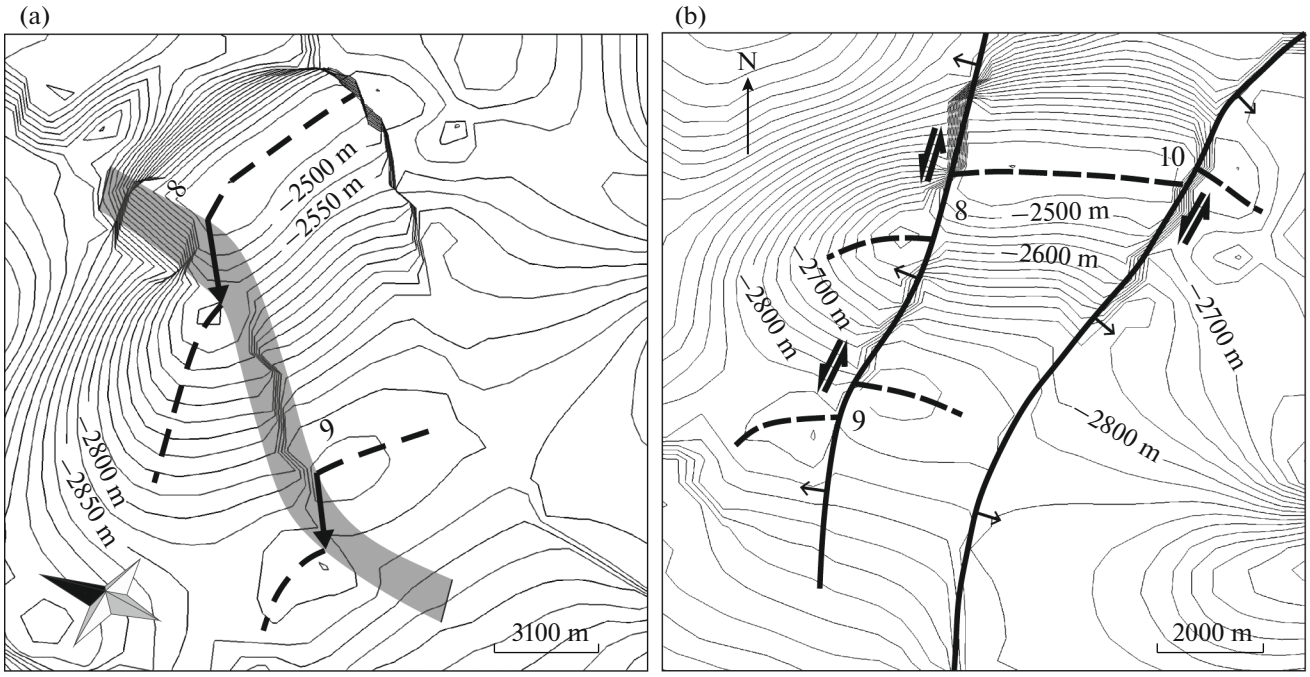

Fig. 7. Determination of slip vector from seismic horizon R_2: (a) view at angle to seismic horizon with fault plane shown in gray; (b) view from above. Numbers of measurements correspond to analogous ones in Fig. 6. Dashed line indicates trace of axial surface; black arrow denotes slip vector.

or compression (σ_1), intermediate axis (σ_2), and axis of minimum stress or deviatoric tension (σ_3).

The quasiprimary stresses method is based on the regularities of destruction of fractured rocks and on the criteria of strength on the largest tangential stresses [14, 16, 29]. The essence of this method is that each slip vector (disregarding whether it was a slickenline at a crack or a documented displacement along a large fault) corresponds to a local stress state where the axes of maximum stress and deviatoric tension are in one plane running through the slip vector perpendicular to the fault plane and are oriented at an angle of 45° to the slip vector. After this information is collected on all available slip vectors, it is processed by statistical methods to obtain the orientations of the main stress axes. This method was developed independently by V.D. Parfenov [14] and J. Angelier [32]; however, implementation of the method in a form of simple-to-use software (FaultKinWin) was proposed only by R. Allmendinger et al. [31, 41]. A shortcoming of this method is the assumption that the compression and deviatoric tension axes are always oriented at 45° to the slip vector. Such a condition is satisfied only on average, whereas individual measurements show angles differing from this value; as well, this is not always valid in the case when faults with similar orientation dominate. For example, if only a sole fracture system is clearly identified in the strike-slip zone due to some reasons (e.g., Riedel fractures or coupled Riedel fractures), then the error in determining the orientations of the compression and deviatoric tension axes can be up to 15°–20°. This is why it is important to have both faults of various orientations and slip vectors and a considerable database for calculations by the FaultKinWin software.

Cataclastic analysis was developed by Yu.L. Rebetsky [16]; it uses common energy statements of contemporary plasticity theory and makes it possible to calculate in one mode both the parameters of stress tensor and augmentation tensor of quasiplastic strain. The obtained stress tensor in every studied volume characterizes the stress field at a given point (local stress state). Using cataclastic analysis, we find the stress state for which every shear from the sampling leads to a decrease in elastic energy (the slip vector and direction of tangential stress on the shear plane should form an acute angle), whereas the maximum release of elastic energy is attained on the aggregate shears of the sampling. Based on these mechanical statements, the software subdivides the available database into homogeneous samplings of shear cracks to enable us to distinguish several stress states from the one initial population of data (formation of two and more homogeneous samplings of cracks). The important difference of the cataclastic analysis from the method of quasiprimary stresses is that (a) tensor of increase of quasiplastic deformation is simultaneously calculated and (b) orientations of main axes of stress tensor are found. Another advantage of cataclastic analysis is that we can calculate the Lode–Nadai coefficient from reduced stresses characterizing the ratio between the main val-

Table 1. Kinematic characteristics of faults

Data point	Fault plane		Slip vector		Angle α	Sense of Slip	Movement amplitude, m		
	dip azimuth	dip angle	trend	plunge			vertical displacement	horizontal displacement	total displacement
Horizon R_2									
1	161	80	72	8	82	TR	250	300	391
2	152	89	62	2	88	TR	50	1003	1004
3	295	89	205	6	85	TR	120	1125	1131
4	269	88	359	10	80	TL	60	344	349
5	286	80	196	2	88	TR	70	1612	1613
6	283	85	14	7	83	NR	110	887	893
7	166	89	76	3	87	NL	50	922	923
8	282	72	194	5	85	NL	100	1247	1251
9	276	72	186	3	87	NL	50	863	864
10	126	88	36	8	82	NL	250	1711	1729
11	179	86	90	20	70	TR	330	896	955
12	170	83	258	16	74	TL	160	559	581
13	170	83	259	9	81	TL	140	871	882
14	193	88	283	3	87	TL	60	1108	1110
15	214	87	305	14	76	NR	120	472	487
16	163	87	253	6	84	TL	90	919	923
17	132	89	222	16	74	TL	140	481	501
18	151	89	241	10	79	TL	80	435	442
19	62	86	333	15	75	TR	210	763	792
Horizon R_3									
1	311	81	41	7	83	TL	120	933	941
2	163	59	76	6	83	TR	200	1940	1950
3	324	78	139	23	66	TL	260	620	672
4	360	87	271	27	63	TR	500	385	631
5	28	88	118	60	29	TL	600	336	687

Table 1. (Contd.)

Data point	Fault plane		Slip vector		Angle α	Sense of Slip	Movement amplitude, m		
	dip azimuth	dip angle	trend	plunge			vertical displacement	horizontal displacement	total displacement
6	24	82	109	32	57	TL	260	419	493
7	282	72	192	10	80	NL	120	664	675
8	276	72	188	7	83	NL	40	300	303
9	124	88	34	13	77	NL	110	495	507
10	277	85	188	13	77	TR	80	341	350
11	80	88	169	17	73	NR	190	614	642
12	207	89	297	18	72	NR	280	859	903
13	210	87	120	15	75	TR	150	545	566
14	193	80	282	8	84	TR	80	545	551
15	178	88	358	10	80	TL	450	2603	2642
16	151	80	65	21	69	TR	400	774	871
17	144	71	225	24	65	TL	360	808	885
18	174	85	87	33	57	TR	860	947	1280
19	164	86	76	24	66	TR	680	1547	1690
20	134	73	216	22	66	TL	510	1271	1370
21	165	88	76	26	64	TR	270	590	649
22	185	72	104	26	63	TR	580	1166	1302
23	121	73	37	20	69	TR	140	383	408
24	115	73	30	15	74	TR	110	402	417
25	204	88	114	7	83	NL	170	1415	1425
26	196	88	107	33	57	TR	370	565	675
27	342	82	254	17	73	TR	250	815	853
28	156	79	240	27	63	TR	190	331	382
29	31	89	121	1	89	NR	50	1455	1456

Table 1. (Contd.)

Data point	Fault plane		Slip vector		Angle α	Sense of Slip	Movement amplitude, m		
	dip azimuth	dip angle	trend	plunge			vertical displacement	horizontal displacement	total displacement
Horizon R_4									
1	156	61	70	8	81	TR	350	2517	2541
2	156	61	68	4	85	TR	220	3581	3588
3	156	61	67	2	88	TL	60	3433	3434
4	156	61	245	1	89	TL	80	2960	2961
5	312	82	40	17	73	TL	160	580	602
6	330	82	59	7	83	TL	300	2514	2532
7	330	82	59	5	85	TL	250	3450	3459
8	294	82	23	7	83	TL	60	482	486
9	173	74	248	42	45	NR	950	1048	1414
10	279	86	7	27	63	TR	310	1139	1180
11	177	82	88	10	80	NL	350	2040	2070
12	147	74	51	19	70	TL	530	1552	1640
13	160	53	243	9	78	TL	250	1568	1588
14	102	58	186	8	80	TL	100	636	644
15	14	83	100	32	58	TL	450	719	848
16	320	83	47	23	67	TL	550	1298	1410
17	3	66	280	16	73	TR	450	1320	1395
18	216	89	103	18	72	TR	270	820	863
19	192	81	103	8	82	TR	200	1273	1289
20	196	79	282	17	73	TL	300	927	974
21	184	71	105	22	60	TL	350	837	907
22	136	83	51	51	52	TL	830	949	1261
23	283	84	194	15	75	NL	90	331	343
24	123	89	33	5	85	NL	100	1100	1105
25	168	89	258	3	87	TL	50	969	970
26	179	88	90	44	46	TR	850	899	1237
27	116	89	26	23	67	TL	250	580	631

Table 1. (Contd.)

Data point	Fault plane		Slip vector		Angle α	Sense of Slip	Movement amplitude, m		
	dip azimuth	dip angle	trend	plunge			vertical displacement	horizontal displacement	total displacement
28	299	86	211	27	63	NL	200	392	440
29	154	86	242	27	63	TL	1480	2861	3221
30	322	88	232	9	81	TL	230	1420	1439
31	358	83	81	45	45	TL	1180	1190	1676
32	341	83	251	2	88	TL	50	1464	1465
33	31	89	301	10	44	TR	180	981	997
34	147	87	236	15	75	NR	750	2856	2953
35	147	87	235	19	70	NR	950	1428	1715
36	330	72	50	29	60	NR	250	451	516
37	331	73	52	27	61	NR	350	665	751
38	332	74	55	21	69	NR	200	516	553
39	200	78	110	2	88	TL	90	2142	2144
40	339	89	69	12	78	TL	70	343	350
41	334	68	61	5	85	TL	90	1006	1010
42	115	88	25	12	86	NL	110	503	515
43	306	89	216	15	75	TR	270	1012	1047
44	57	89	327	12	78	TR	70	328	336
45	115	89	204	8	82	TR	100	721	728
46	120	89	209	2	88	TR	30	970	970
47	33	89	122	16	74	TL	650	1983	2087
48	42	88	131	19	69	TL	500	1416	1502

Angle α is acute angle between slip vector and direction of fault plane dipping (see Fig. 3). Abbreviations of slip types: TR, reverse fault with right-lateral strike-slip component; TL, reverse fault with left-lateral strike-slip component; NR, normal fault with right-lateral strike-slip component; NL, normal fault with left-lateral strike-slip component.

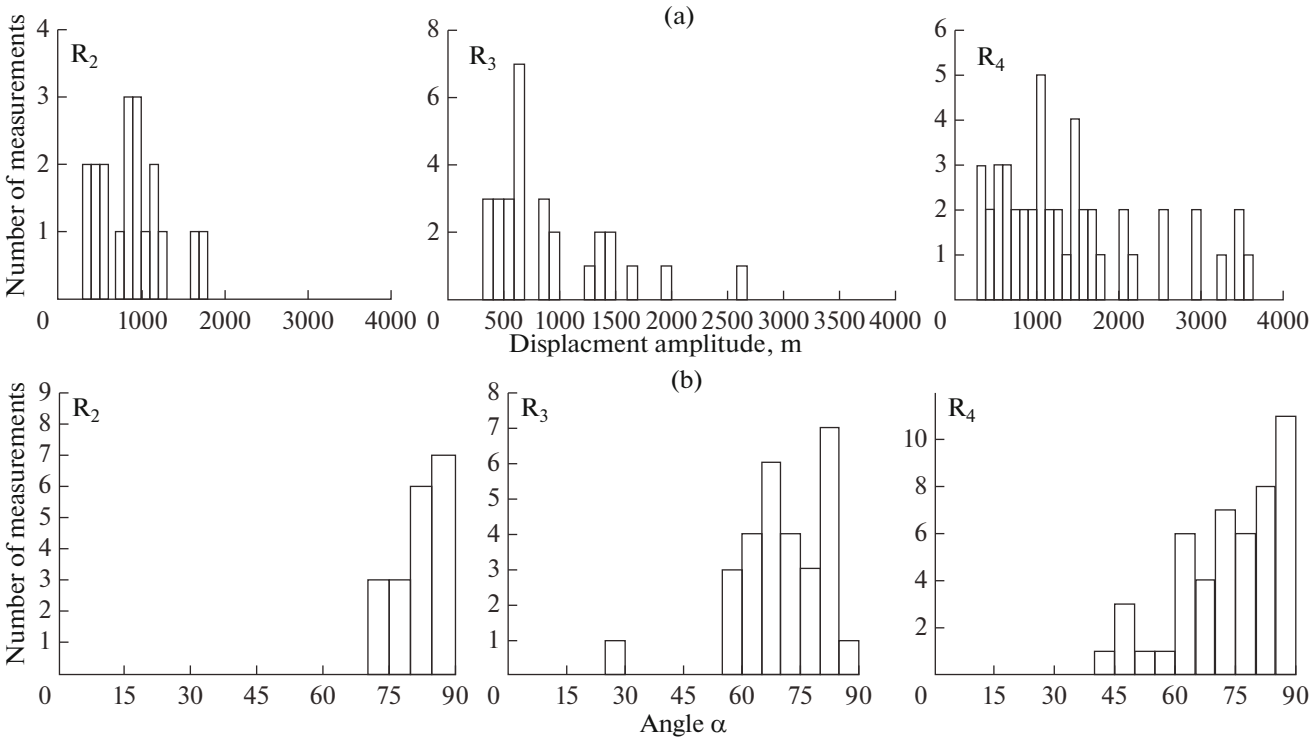

Fig. 8. Characteristics of slip vector on R_4, R_3, and R_2 seismic horizons: (a) column charts showing distribution of total displacement amplitudes; (b) column charts showing distribution of angle α.

ues of tensor and axes of the stress ellipsoid; this ratio is used to subdivide the initial data sampling into generations of different orders. For simple shear, the Lode–Nadai coefficient is 0; as its value approaches +1, the shape of the stress ellipsoid becomes similar to an oblate spheroid (uniaxial compression), whereas if its value approaches –1, the shape of the stress ellipsoid becomes similar to an oblong ellipsoid (uniaxial extension). Cataclastic analysis has been successfully implemented in the StressGeol software developed at the Laboratory of Tectonophysics, Institute of Physics of the Earth, Russian Academy of Sciences, by Yu.L. Rebetsky [16]. It should be noted that the StressGeol program works with a set of measurements whose kinematic characteristics agree with each other according to different criteria, whereas the FaultKinWin program utilizes singular measurements. Joint application of these two programs, which are based on different theoretical methods, makes it possible to control the quality of the initial database. In particular, similar orientations of the stress axes obtained by data processing in the FaultKinWin and StressGeol programs give grounds to believe that the sampling does not contain any dominant system of parallel cracks (e.g., Riedel shears related to the same fault) and any internal irregularities.

RESULTS OF STRUCTURAL DATA PROCESSING

Kinematic Characteristics of Faults

Based on the analysis of structural maps of seismic horizons and related faults within the study area, the most commonly developed are faults of ENE–WSW and NNE–SSW trends. The faults in the study area contain both normal and reverse faulting components. A strike-slip component is observed in the majority of faults, but there are no consistent distribution patterns for left- and right-lateral strike-slips. In general, faults are identified as steeply dipping planes with angles from 70° to 90°, but there are also faults with more gentle dipping angles of 50° to 60°.

Analysis of the kinematic characteristics of faults has shown that the number of folded structures from whose displacements we could measure slip vectors decreases upsection: 48 for the R_4 horizon, 29 for the R_3 horizon, and 19 for the R_2 horizon. A similar trend is obtained from comparison of the total motion amplitudes from faults (Fig. 8a), which change from approximately 350 to 1730 m for the R_2 horizon, whereas the largest motion amplitudes for the R_3 and R_4 horizons are 2640 and 3590 m, respectively. With the overall approximate character of calculating the average values, average values of total displacements

for faults identified at different seismic horizons are about 885 m for the R_2 horizon, 903 m for R_3, and 1412 m for R_4, which also indicates an increase in the motion amplitudes downsection. A similar correlation is obtained from the average values of the vertical displacement components: approximately 130 m for R_2, 290 m for R_3, and 345 m for R_4. The characteristics of the relationship between the strike-slip and reverse faulting components of faults (α angle in the fault plane) identified at the R_2, R_3, and R_4 seismic horizons (see Fig. 8b) makes it possible to identify two stages of their formation. For all faults, except for one at the R_3 horizon and one at the R_4 horizon, the strike-slip component is predominant, but the quantitative ratio between strike-slip and either normal or reverse faulting component significantly differs depending on the particular seismic horizon. For the faults identified at the R_3 and R_4 seismic horizons, reverse faulting component is quite significant, whereas the faults identified at the R_2 horizon have a dominant strike-slip component and for the majority of faults, the orientation of the slip vector in the fault plane differs from the horizontal by less than 10°. Thus, in the time interval after the accumulation of the layers limited by the R_3 seismic horizon, but before the accumulation of the layers limited by the R_2 seismic horizon, the essential change in kinematic characteristics of the faults occurred, so we can distinguish two stages of evolution of the faults: (1) predominantly oblique reverse faulting, which occurred earlier and was clearly manifested in the kinematic characteristics of faults at the R_3 and R_4 seismic horizons, and the (2) strike-slip stage, which occurred later and was dominant for the faults identified at the R_2 seismic horizon. It should be noted that the average total amplitudes of displacements along the faults for the R_3 and R_2 seismic horizons are close to each other (885 and 903 m, respectively), indicating that the most intense deformations took place after accumulation of the rocks confined to the R_2 seismic horizon, whereas the new identified tectonic event occurred only in small reverse and/or normal displacements along the faults. Taking into account the noticeable predominance of reverse faults over normal faults, the identified tectonic event was most likely related to compressional strains.

Orientations of the Main Stress Axes and Shape of the Stress Ellipsoid

From the initial database, the orientations of the main stress axes were calculated by the StressGeol program, which can distinguish several generations that correspond to different formation stages of faults. For comparison, the orientations of the main stress axes for each generation were also calculated by the FaultKinWin program. As data processing by the StressGeol program shows, all faults identified at the R_2, R_3, and R_4 seismic horizon demonstrate the presence of two generations of faults. The first-generation faults at all seismic horizons have similar stress state parameters, with the axis of compression characterized by subhorizontal occurrence and submeridional orientation at the R_3 and R_4 seismic horizons, while there is a NNE orientation at the R_2 horizon. The axis of deviatoric tension is also subhorizontal and oriented perpendicular to the axis of compression. The second-generation faults for all seismic horizons are also characterized by subhorizontal occurrence of the axes of compression and axes of deviatoric tension, but with inversed orientations of these axes at the R_2 and R_4 seismic horizons; an inversion and a small rotation is also observed for the R_3 seismic horizon (Fig. 9). Thus, on the surfaces of all seismic horizons, the main stress axes have similar orientations in each generation, where the intermediate axes (σ_2) are subvertical and the axes of deviatoric tension (σ_3) and compression (σ_1) are subhorizontal, which are all indications of a strike-slip setting [4, 23]. A setting similar to a strike-slip setting is indicated by Lode–Nadai coefficient values close to 0, although weakly positive values characterizing stress states calculated for the first-generation faults at the R_3 and R_4 seismic horizons also indicate the presence of a thrusting component in the stress field (Table 2).

Taking into consideration that 54% of measurements show stress states with a submeridionally oriented axis of compression (first generation), whereas 46% of measurements show a field with a sublatitudinal axis of compression (second generation), the first generation seemingly corresponds to the major deformation stage, whereas the second generation reflects a minor deformation stage, with manifestation of less intense deformations. Note that there are no reliable data on the age relationships between the major and minor stages of pre-Vendian deformations. Nevertheless, their relative age can be inferred based on the following speculations. All information about the stress state parameters is obtained from the fault kinematics data (i.e., on the directions of displacments along fault planes). If the most intense deformations were the youngest, then the displacements corresponding to this stage would be identified on all faults and mask displacements corresponding to the less intense deformations. In the considered examples (see Fig. 9), we can distinguish with high confidence two generations of stress states, and this gives grounds to believe that the less intense deformations (second generation, 46% of measurements) overlapped more intense ones (first generation, 54% of measurements). Thus, we can distinguish two deformation stages in pre-Vendian time: the earlier and more intense stage is characterized by a submeridional axis of compression, whereas deformations of the younger and less intense stage have a WNW-oriented axis of compression.

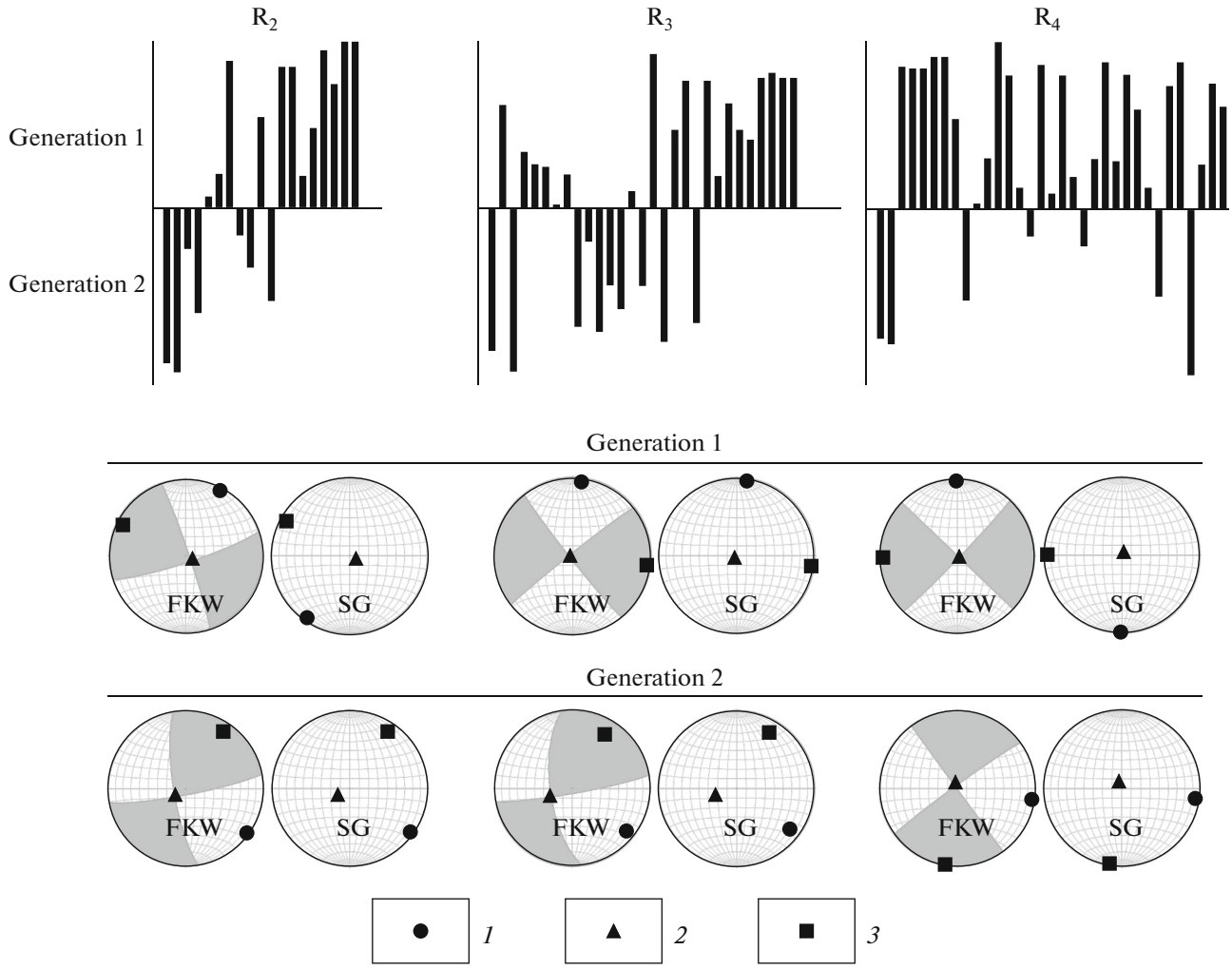

Fig. 9. Stress state parameters on R_4, R_3, and R_2 seismic horizons. Column charts in top panel show distribution of population of slip vectors between generations by StressGeol program; column length denotes probability of reference to respective generation for a given vector. Circles in bottom panel show orientations of main stress axes for two generations of slip vectors n R_4, R_3, and R_2 seismic horizons. (*1*) Axis of compression (σ_1), (*2*) intermediate axis (σ_2), (*3*) axis of deviatoric tension (σ_3). White segment shows the compression, dark shows the extension. Lower hemisphere, Schmidt net.: SG, calculation in StressGeol software; FKW, in FaultKinWin software.

GEODYNAMIC INTERPRETATION OF THE OBTAINED RESULTS

Our study on evaluation of the stress state and taking into consideration data on regional stratigraphy allows us to reconstruct the main tectonic events of the pre-Vendian evolution of the study area (Fig. 10).

The earliest interpreted tectonic event is related to the basement of the Kuyumba rift and the trough of Riphean age related to it (see Fig. 10a). This stage corresponds to intrusion of sills with Ar–Ar ages varying from 1430 ± 14 to 1513 ± 27 Ma [25, 26]. Among the sedimentary rocks, the dominant ones are sandstones and organic-enriched argillites of the Zelendukon, Verdshe, and Madra strata (see Fig. 2), which is typical pf rift sedimentary basins [28]. During this event, the frameworks of faults were formed; these faults control the further evolution of the region. Orientations of the major faults are from northeast to sublatitudinal [26].

The evolutionary stage following rifting covers a considerable part of the Middle Riphean and is characterized by predominantly carbonate sedimentation, which indicates relatively quiescent tectonic settings (this is verified by the similarity of the kinematic characteristics of faults identified at the R_3 and R_4 seismic horizons). The sedimentary basin widened beyond the limits of grabens to gradually prograde northeast and south [27]. The quiet evolution of the sedimentary basin was interrupted by a short-term deformation phase when small-amplitude faults formed (Fig. 10b), as indicated by the difference in the fault kinematics at the R_3 and R_4 horizons compared to the R_2 horizon (see Fig. 8). The common presence of reverse faults

Table 2. Results of calculating stress state parameters for R_2, R_3, and R_4 seismic horizons in FaultKinWin program

Seismic horizon	Generation 1						
	deviatoric tension axis σ_3		intermediate axis, σ_2		compression axis σ_1		μ_s
	trend	plunge	trend	plunge	trend	plunge	
R_2	296	8	135	82	27	3	−0.05
R_3	97	4	270	86	7	0	0.16
R_4	269	2	131	87	359	2	0.2
Seismic horizon	Generation 2						
	deviatoric tension axis σ_3		intermediate axis, σ_2		compression axis σ_1		μ_s
	trend	plunge	trend	plunge	trend	plunge	
R_2	35	14	232	76	125	4	0
R_3	34	20	248	66	128	12	0.05
R_4	189	2	319	87	99	2	0.1

μ_s is the Lode–Nadai coefficient.

indicates that the normal faults that have been formed at the rifting stage underwent partial inversion. In terms of stratigraphy, this event was marked by pre-Vingol'da washing. According to the correlation scheme proposed by E.M. Khabarov [24, 25], its age varies from 1080 to 1000 Ma, which is noticeably older than the tectonic events revealed in the Yenisei Range, and its geodynamic nature remains disputable.

The most intense tectonic events in the study area occurred after the accumulation of Riphean rocks (see Fig. 2) but before deposition of Vendian sedimentary rocks. In this period, the onset of the main structural elements observed at the pre-Vendian surface took place (in particular, those at the R_2, R_3, and R_4 seismic horizons). As follows from the analysis given above, the per-Vendian tectonic event consists of two stages (see Figs. 10c and 10d). The earlier and the more intense first stage of deformations was characterized by the submeridionally oriented axis of compression and by the predominance of strike-slip displacements (see Fig. 10c). However, as is seen from the values of Lode–Nadai coefficient (see Table 2), a reverse faulting component is also present, indicating probable inversion of pre-existing normal faults. At the second stage of pre-Vendian deformation, strike-slip tectonics played a leading role. The axis of compression is oriented sublatitudinally, which demonstrates inversion of strike-slip displacements along faults (Fig. 10d). Although the ages of deformation stages were not revealed, taking into account the age of tectonic events in the Yenisei Range, we can suggest that the first stage of pre-Vendian deformations in the study area could be a response to the earliest collisional events and about 760–750 Ma in age, whereas the second stage of pre-Vendian deformations corresponds to the final stages of evolution of the active margin ca. 685–600 Ma ago.

The cause of stress field inversion in the study area was not revealed. Analogous stress field inversions accompanied by a change in direction of displacements along faults to the opposite have been documented in various regions (see, e.g., [2, 10, 22, 30, 38, 45]).

Stress field inversion is usually attributed to changes in plate kinematics; however, the available paleomagnetic data [3, 13] are too ambiguous to make any reliable conclusion about Siberian Plate kinematics during the existence of an active margin on its southwest (present-day coordinates) ca. 900–600 Ma ago. Additionally, it must be emphasized that both stages of deformation in the study area are characterized by a strike-slip setting, whereas the role of strike-slip in the Yenisei Range tectonics remains vague.

CONCLUSIONS

At present, studies of the stress state parameters of closed territories have relatively few methods to determine the indicators of tectonic stress fields for further calculation of stress tensor. Our research shows the reliable applicability of the method of stress state reconstruction from 3D seismic data, where the indicator of tectonic stresses is the vector of displacement along faults, with the spatial orientation of this slip (e.g., slickensides or slickenlines) used to calculate the orientation of the main stress axes and shape of the stress ellipsoid. The main results of this method are as follows:

(1) Analysis of the kinematic characteristics of faults identified in the structural maps of the R_2, R_3, and R_4 seismic horizons shows that components of displacements in both lateral (strike-slip) and vertical (reverse or normal faults) directions are presented. The earliest change in the kinematic characteristics of

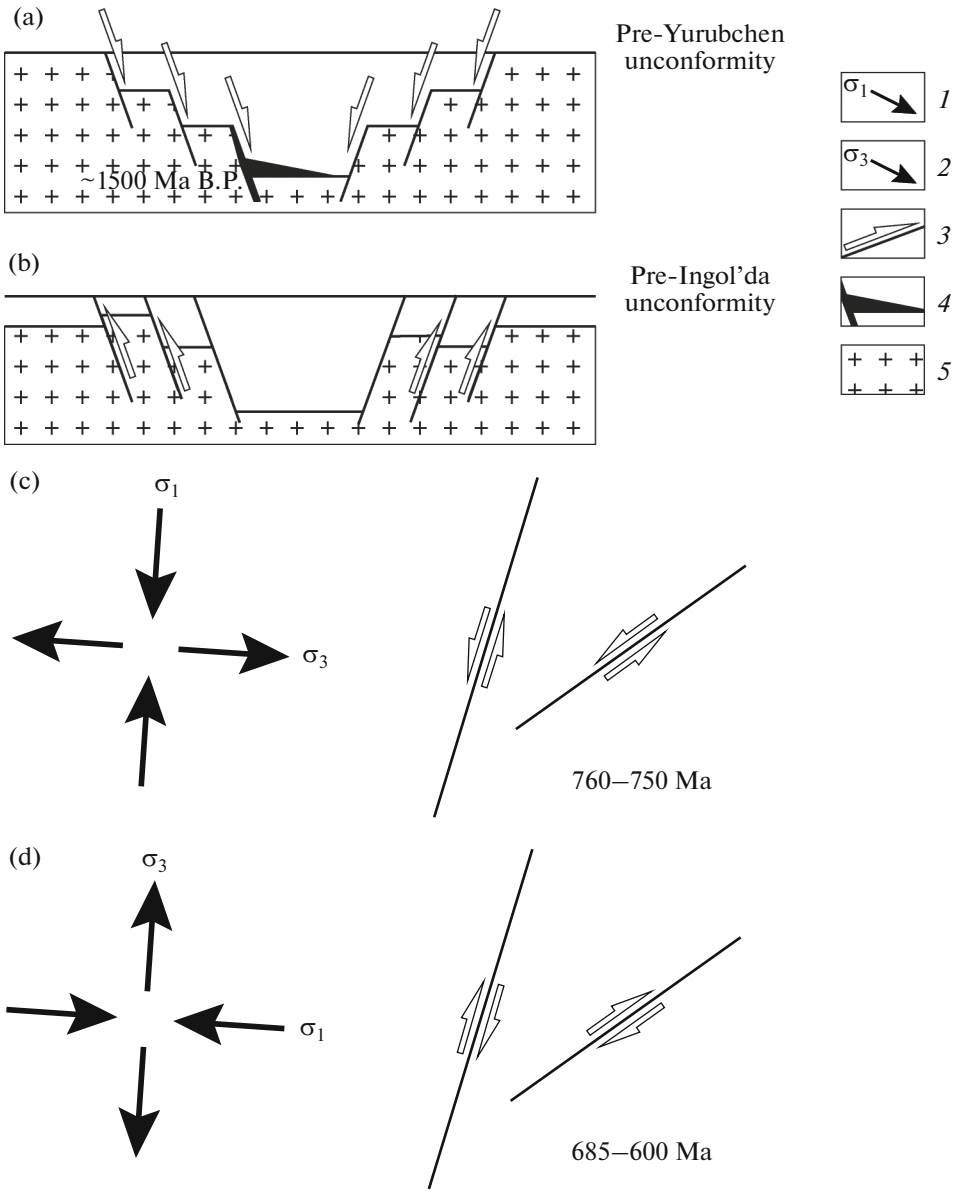

Fig. 10. Tectonic evolution of northern slope of Baikit anteclise. Stages: (a) nucleation of rift; (b) inversion of displacements along faults in pre-Vingol'da time; (c) first stage of pre-Vendian deformations; (d) second stage of pre-Vendian deformations. (*1*) Axis of compression (σ_1); (*2*) axis of deviatoric tension(σ_3); (*3*) directions of slips along faults; (*4*) basic-rock intrusions of ca. 1500 Ma in age; (*5*) Siberian Craton basement.

faults is associated with an event that occurred in the pre-Vingol'da time.

(2) Two stages of deformations during the pre-Vendian folding have been revealed in the region: the most intensive stage with prevalence of thrust and strike-slip faults at north-northeast orientation of an axis of the main compression, and second stage with prevalence of strike-slip faults at the west-northwest orientation of an axis of the main compression. These stages are correlated with the tectonic events which were taking place during evolution of the active southwest margin of the Siberian platform.

ACKNOWLEDGMENTS

The initial seismic data were provided by LLC GAZPROMNEFT STC. The authors are grateful to Yu.L. Rebetsky and L.A. Sim (both at the Institute of Physics of the Earth, Russian Academy of Sciences, Moscow) for advice on the developed method and

discussion of the stress state reconstruction methods. The authors also thank the reviewer for valuable remarks that improved the publication.

REFERENCES

1. L. M. Balakina, A. V. Vvedenskaya, I. V. Golubeva, L. A. Misharina, and E. I. Shirokova, *Elastic Stress Field in the Solid Earth and Earthquake Focal Mechanisms* (Nauka, Moscow, 1972) [in Russian].
2. V. E. Verzhbitsky, S. D. Sokolov, and M. I. Tuchkova, "Present-day structure and stages of tectonic evolution of Wrangel Island, Russian Eastern Arctic region," Geotectonics **49**, 165–192 (2015).
3. V. A. Vernikovsky, A. Yu. Kazansky, N. Yu. Matushkin, D. V. Metelkin, and J. K. Sovetov, "The geodynamic evolution of the folded framing and the western margin of the Siberian craton in the Neoproterozoic: Geological, structural, sedimentological, geochronological, and paleomagnetic data," Russ. Geol. Geophys. **48**, 502–519 (2009).
4. M. V. Gzovsky, *Fundamentals of Tectonophysics* (Nauka, Moscow, 1975) [in Russian].
5. A. S. Gladkov and O. V. Lunina, "Fractures in Late Cenozoic sediments: New possibilities for structural analysis," Dokl. Earth Sci. **399**, 1071–1073 (2004).
6. O. I. Gushchenko, "Analysis of orientations of shear tectonic displacements and their tectonic displacements: Tectonophysical interpretation when paleostress reconstruction," Dokl. Akad. Nauk SSSR **210**, 331–334 (1973).
7. O. I. Gushchenko, "Method of kinematic analysis of destruction-related structures when reconstructing tectonic stress fields," in *Stress Fields in the Lithosphere*, Ed. by A. S. Grigor'ev and D. N. Osokina (Nauka, Moscow, 1979), pp. 7–25.
8. O. V. Lunina, A. S. Gladkov, I. S. Novikov, A. R. Agatova, E. M. Vysotsky, and A. A. Emanov, "Seismotectonic deformations and stress fields in the fault zone of the 2003 Chuya earthquake, M_s = 7.5, Gorny Altai," Geotectonics **40**, 208–224 (2006).
9. A. V. Marinin and L. A. Sim, "The contemporary state of stress and strain at the western pericline of the Greater Caucasus," Geotectonics **49**, 411–424 (2015).
10. Yu. A. Morozov, "Cyclicity of kinematic inversions in mobile belts in the light of lunar–terrestrial interaction," Geotectonics **38**, 17–42 (2004).
11. A. N. Moskalenko, A. K. Khudoley, V. V. Zhukov, V. Yu. Demin, and A. V. Verin, "Reconstruction of kinematic characteristics of faults and paleostress field for the Urman-Archa area," Neftegaz. Geol. Teor. Prakt., No. 5, 1–16 (2015).
12. P. N. Nikolaev, "The technique of statistical analysis of fractures and the reconstruction of tectonic stress fields," Izv. Vyssh. Uchebn. Zaved., Geol. Razved., No. 12, 103–115 (1977).
13. V. E. Pavlov, A. V. Shatsillo, and P. Yu. Petrov, "Paleomagnetism of the Upper Riphean deposits in the Turukhansk and Olenek uplifts and Uda pre-Sayan region and the Neoproterozoic drift of the Siberian Platform," Izv., Phys. Solid Earth **51**, 716–747 (2015).
14. V. D. Parfenov, "On the technique of tectonophysical analysis of geological structures," Geotektonika, No. 1, 60–72 (1984).
15. Yu. L. Rebetsky, "Review of methods for reconstructing tectonic stresses and seismotectonic deformations," in *Tectonophysics Today*, Ed. by V. N. Strakhov and Yu. G. Leonov (Ob"ed. Inst. Fiz. Zemli Ross. Akad. Nauk, Moscow, 2002), pp. 227–243.
16. Yu. L. Rebetsky, *Tectonic Stresses and Rigidity of Natural Rock Massifs* (Akademkniga, Moscow, 2007) [in Russian].
17. Yu. L. Rebetsky, O. A. Kuchai, and A. V. Marinin, "Stress state and deformation of the Earth's crust in the Altai–Sayan mountain region," Russ. Geol. Geophys. **54**, 206–222 (2013).
18. L. A. Sim, "Determination of the regional stress field from local stress fields in particular sites: Case study of the junction area between the Mezen syeclise and Middle Timan Range," Izv. Vyssh. Uchebn. Zaved., Geol. Razved., No. 4, 35–40 (1982).
19. L. A. Sim, "Studying of tectonic stresses from geological indicators (methods, results, recommendations)," Izv. Vyssh. Uchebn. Zaved., Geol. Razved., No. 10, 3–22 (1991).
20. L. A. Sim, "Influence of global tectogenesis on the recent stress state of European platforms," in *M. V. Gzovsky and Advances in Geophysics*, Ed. by Yu. G. Leonov (Nauka, Moscow, 2000), pp. 326–350.
21. L. A. Sim, N. A. Sycheva, V. N. Sychev, and A. V. Marinin, "The pattern of the paleo- and present-day stresses of Northern Tien Shan," Izv., Phys. Solid Earth **50**, 378–392 (2014).
22. S. N. Sychev and K. V. Kulikova, "Structural evolution of the Main Ural Fault Zone in the western framework of the Voikar–Synya ophiolite massif," Geotectonics **46**, 427–434 (2012).
23. T. Uemura and S. Mizutani, *Geological Structures* (Wiley, New York, 1984).
24. E. M. Khabarov, "Carbonate sedintation in the Meso-Neoproterozoic basins in southern East Siberia and some problems of evolution of reef formation in the Precambrian," Russ. Geol. Geophys. **52**, 1140–1153 (2011).
25. E. M. Khabarov, V. A. Ponomarchuk, I. P. Morozova, I. V. Varaksina, and S. V. Saraev, "Variations in the sea level and isotopic composition of carbonate carbon in the Riphean basin at the western margin of the Siberian Craton (Baikit anteclise)," Geol. Geofiz., No. 3, 211–239 (2002).
26. V. V. Kharakhinov and S. I. Shlenkin, *Petroleum-Bearing Potential of Precambrian Sequences in East Siberia: Case Study of the Kuyumba-Yurubchen-Tokhoma Petroleum Accumulation Areal* (Nauchn. Mir, Moscow, 2011) [in Russian].
27. T. N. Kheraskova, S. A. Kaplan, and V. I. Galuev, "Structure of the Siberian Platform and its western margin in the Riphean–Early Paleozoic," Geotectonics **43**, 115–132 (2009).
28. A. K. Khudoley, *Continental Rifting and Passive Margins: Tectonics and Evolution of Sedimentary Basins* (St. Petersburg Gos. Univ., St. Petersburg, 2004) [in Russian].

29. S. I. Sherman and Yu. I. Dneprovskii, *Stress Fields in the Crust and Geological-Structural Methods of Their Study* (Nauka, Novosibirsk, 1989) [in Russian].

30. D. V. Alexeiev, H. E. Cook, V. M. Buvtyshkin, and L. Y. Golub, "Structural evolution of the Ural–Tien Shan junction: A view from Karatau ridge, South Kazakhstan," C.R. Geosci. **341**, 287–297 (2009).

31. R. W. Allmendinger, N. C. Cardozo, and D. Fisher, *Structural Geology Algorithms: Vectors & Tensors* (Cambridge Univ. Press, Cambridge, 2012).

32. J. Angelier, "Tectonic analysis of fault slip data sets," J. Geophys. Res., B **89**, 5835–5848 (1984).

33. T. Engelder and P. A. Geiser, "On the use of regional joint sets as trajectories of paleostress fields during the development of the Appalachian Plateau, New York," J. Geophys. Res., B **94**, 6319–6341 (1980).

34. A. P. Gartrell and M. Lisk, "Potential new method for paleostress estimation by combining three-dimensional fault restoration and fault slip inversion techniques: First test on the Skua Field, Timor Sea," in *Evaluating Fault and Cap Rock Seals*, Vol. 2 of *AAPG Hedberg Series*, Ed. by P. Boult and J. Kaldi (AAPG, 2005), pp. 23–36.

35. M. Gharbi, O. Bellier, A. Masrouhi, and N. Espurt, "Recent spatial and temporal changes in the stress regime along the southern Tunisian Atlas front and the Gulf of Gabes: New insights from fault kinematics analysis and seismic profiles," Tectonophysics **626**, 120–136 (2014).

36. Y. Hashimoto, M. Eida, and Y. Ueda, "Changes in paleostress state along a subduction zone preserved in an on-land accretionary complex, the Yokonami mélange in the Cretaceous Shimanto Belt, Kochi, southwest Japan," Tectonics **33**, 2045–2058 (2014).

37. H. A. Khair, D. Cooke, and M. Hand, "Paleo stress contribution to fault and natural fracture distribution in the Cooper Basin," J. Struct. Geol. **79**, 31–41 (2015).

38. A. K. Khudoley and S. D. Sokolov, "Structural evolution of the northeast Asia continental margin: An example from the western Koryak fold and thrust belt (northeast Russia)," Geol. Mag. **135**, 311–330 (1998).

39. G. G. Lash and T. Engelder, "Tracking the burial and tectonic history of Devonian shale of the Appalachian Basin by analysis of joint intersection style," Geol. Soc. Am. Bull. **121**, 265–277 (2009).

40. R. J. Lisle and R. J. Walker, "The estimation of fault slip from map data: The separation-pitch diagram," Tectonophysics **583**, 158–163 (2013).

41. R. Marrett and R. Allmendinger, "Kinematic analysis of fault-slip data," J. Struct. Geol. **12**, 973–986 (1990).

42. A. P. Morris, R. N. McGinnis, and D. A. Ferrill, "Fault displacement gradients on normal faults and associated deformation," AAPG Bull. **98**, 1161–1184 (2014).

43. Yu. L. Rebetsky, A. Yu. Polets, and T. K. Zlobin, "The state of stress in the Earth's crust along the northwestern flank of the Pacific seismic focal zone before the Tohoku earthquake of 11 March 2011," Tectonophysics **685**, 60–86 (2016).

44. B. A. van der Pluijm and S. Marshak, *Earth Structures: An Introduction to Structural Geology and Tectonics*, 2nd ed. (New York: W. W. Norton & Company, 2004).

45. X. Xu, S. Tang, and S. Lin, "Paleostress inversion of fault-slip data from the Jurassic to Cretaceous Huangshan Basin and implications for the tectonic evolution of southeastern China," J. Geodyn. **98**, 31–52 (2016).

Reviewer: T.N. Kheraskova

Translated by N. Astafiev